Bioactive Materials 5 (2020) 153–163

Contents lists available at ScienceDirect

Bioactive Materials

journal homepage: http://www.keaipublishing.com/biomat

In vitro corrosion resistance of layer-by-layer assembled polyacrylic acid multilayers induced Ca–P coating on magnesium alloy AZ31

Lan-Yue Cui[a], Shen-Cong Cheng[a], Lu-Xian Liang[a], Jing-Chao Zhang[a], Shuo-Qi Li[a], Zhen-Lin Wang[c], Rong-Chang Zeng[a,b,*]

[a] College of Materials Science and Engineering, Shandong University of Science and Technology, Qingdao, 266590, China
[b] School of Materials Science and Engineering, Zhengzhou University, Zhengzhou, 450002, China
[c] College of Materials Science and Engineering, Chongqing University of Technology, Chongqing, 400065, China

ARTICLE INFO

Keywords:
Magnesium alloy
Layer-by-layer assembly
Biomineralization
Calcium phosphate
Coating
Corrosion

ABSTRACT

Biodegradable magnesium (Mg)-based alloys have aroused great concern owing to their promising characteristics as temporary implants for orthopedic application. But their undesirably rapid corrosion rate under physiological conditions has limited the actual clinical application. This study reports the use of a novel biomimetic polyelectrolyte multilayer template, based on polyvinylpyrrolidone (PVP) and polyacrylic acid (PAA) via layer-by-layer (LbL) assembly, to improve the corrosion resistance of the alloy. Surface characterization techniques (field-emission scanning electron microscopy, Fourier transform infrared (FTIR) spectrophotometer and X-ray diffractometer) confirmed the formation of biomineralized Ca–P coating on AZ31 alloy. Both hydrogen evolution and electrochemical corrosion tests demonstrated that the corrosion protection of the polyelectrolyte-induced Ca–P coating on AZ31 alloy. The formation mechanism of biomineralized Ca–P coating was proposed.

1. Introduction

Biodegradable magnesium (Mg)-based alloys with close density and mechanical properties to the natural bone, have received great consideration owing to their promising characteristics as temporary implants for orthopedic application, which have the ability to degrade inside the human body to avoid the second surgery [1–3]. However, the main drawback of employing Mg for orthopedic application is the high degradation rate along with the generation of hydrogen gas and boom in alkalinity of body fluid [4–6]. Surface modification is a viable option to control Mg degradation rate and enhance its bioactivity for accelerating the healing process [2,7–9].

As the main composition of bones, calcium-bearing phosphate (Ca–P) coatings have been paid more attentions due to their superior biocompatibility and corrosion resistance, which can be fabricated through chemical conversion [10–12], cathodic electrodeposition (EDP) [13–15] and sol-gel [16,17], etc. And hydrothermal deposition (HDP) is a more economical and convenient method to prepare crystalline Ca–P coating on metallic materials [18–20]. It is, however, difficult to obtain the coatings of pure calcium orthophosphates on biodegradable Mg and its alloys due to the severe corrosion of Mg substrate in aqueous solutions at elevated temperatures. As a result, the released Mg^{2+} ions may lead to the formation of a corrosion product layer of $Mg(OH)_2$ and substitute for Ca^{2+} ions in the structure of the calcium orthophosphates coatings [21].

In order to improve the purity, compactness and bonding strength of Ca–P coatings, complexing agents, organic and polymer compounds as an inducer or template were used to accelerate the deposition of calcium orthophosphates, based on the molecular recognition. For instance, ethylene diamine tetraacetic acid (EDTA), especially for Na-EDTA [10,22] and Ca-EDTA [23], can coordinate with metallic ions to form stable chelates [22], and thus is often used to construct Ca–P coatings. Ca-EDTA can supply a sufficiently high concentration of Ca^{2+} ions to cause precipitation, and then achieving a highly crystalline coating [24].

The organic and polymer compounds, used in the coating preparation, include peptide, dopamine, glucose, amino acids and protein. Cui et al. [25] showed that a novel biomimetic peptide with triple repeat of a tri-residue sequence (aspartic acid-serine-serine) can direct Ca–P formation on the AZ31B alloys and result in a very different Ca–P crystal structure. Cao et al. [11] formed an arginine-glycine-aspartic acid-cysteine peptide-induced Ca–P coating using a biomimetic

Peer review under responsibility of KeAi Communications Co., Ltd.
* Corresponding author. College of Materials Science and Engineering, Shandong University of Science and Technology, Qingdao, 266590, China.
E-mail addresses: cuily@sdust.edu.cn (L.-Y. Cui), 1194154697@qq.com (S.-C. Cheng), 2275483214@qq.com (L.-X. Liang), 1049074353@qq.com (J.-C. Zhang), lishuoqi@sdust.edu.cn (S.-Q. Li), wzl@cqut.edu.cn (Z.-L. Wang), rczeng@foxmail.com (R.-C. Zeng).

https://doi.org/10.1016/j.bioactmat.2020.02.001
Received 16 December 2019; Received in revised form 2 February 2020; Accepted 2 February 2020

method, which presented an improved anticorrosion ability and cellular responses. That is, many peptides can be used as inducers to obtain Ca–P coatings on Mg alloys, but the peptides tend to lose their activity in alkaline or high temperature environments. Ca–P coatings also can be successfully achieved on Mg alloys through a biomimetic strategy in presence of mussel-inspired polydopamine (PDA) [26,27], but the immersion process of the PDA leads to corrosion of the Mg substrate, which goes against the protection improvement of the composite coating. Glucose was selected by Li et al. to induce a Ca–P coating to enhance the corrosion resistance of pure Mg through the changes between glucose and gluconic acid during hydrothermal process [18]. Noticeably, the uniformity of adsorption directly affects the homogeneity of the obtained Ca–P coatings.

Also, silk fibroin is used to obtain Ca–P coating with the addition of Ca, Sr and P sources. The composite films acted as effective barriers to retard substrate corrosion significantly; and the cytocompatibility and ontogenetic performance of the coated samples were improved [28]. Furthermore, Cui et al. [10,29] exhibited a novel SnO_2-doped Ca–P coating on degradable Mg alloys. SnO_2 nanoparticles, embedded in the coating, enhanced the compactness and crystallization of the coatings and acted as a foreign material to provide heterogeneous nucleation sites for the deposition of Mg^{2+} and Ca^{2+} with PO_4^{3-} ions. But the bonding strength of the obtained Ca–P coating is deficient to be used as bone implants.

Layer-by-layer (LbL) films (or "polyelectrolyte multilayers") are potential templates for the biomimetic deposition of Ca–P coatings for bone tissue engineering by improving the heterogeneous nucleation of Ca–P precipitates and homogeneous deposition of Ca–P coatings [30]. Early on, Ngankam et al. [31] indicated that the poly(ethyleneimine)-(poly(styrene sulfonate)-poly(allylamine hydrochloride))$_2$ (PEI-(PSS-PAH)$_2$) polyelectrolyte multilayers, both negatively or positively charged, led to a decrease of the supersaturating ratio for heterogeneous nucleation of calcium phosphate crystals. Li et al. [32] showed that Ca–P precipitates were successfully deposited on the surface of gelatin/PSS covered polycaprolactone fibers by mineralization, in which gelatin and PSS were immobilized by LbL assembly. Ji et al. [33] constructed a hydroxyapatite (HA) coating with polymeric multilayers based on ciprofloxacin (CIP) and PAH via LbL assembly, obtained a compact flake morphology and high crystallized apatite structure with improved corrosion resistance, controlled drug release, excellent antibacterial activity and suitable cytocompatibility, but the corrosion protection is still limited.

Polyacrylic acid (PAA) exhibits strong muco-adhesive property and good biocompatibility, which can be used as a biomedical material [34]. However, high water swelling property of PAA critically limits its use as a physical barrier to block the penetration of corrosive ions. A (polyvinylpyrrolidone (PVP)/PAA)$_5$ multilayer was formed on AZ31 alloys, but it acted as a skeleton to absorb silane rather than to be a shield to improve the corrosion resistance, and during immersion in Hank's solution, $Ca_3(PO_4)_2$ and HA corrosion products were found, demonstrating a good mineralization effect of the composite coating [35,36]. Thus, PAA may be a good candidate to induce Ca–P coating via molecular recognition with a large amount of carboxyl (-COOH) groups. Adversely, there are some studies indicating that PAA inhibits the growth of HA crystals, and the opposite effects are considered to result from the conformational differences whether they are free in the solution or not [37].

For Mg alloys, current hydrothermal methods have reported Ca–P coatings with non-uniform and porous morphology, due to the hydrogen bubbles formed on the Mg surface and the heterogeneous deposition during the coating process [20,25,38]. Thus, to improve the homogeneity, bonding force and corrosion resistance of the Ca–P coating, an inner (PVP/PAA)$_{5.5}$ polyelectrolyte multilayer was designed to be used as a template to induce the Ca–P composite coating on AZ31 alloy. In addition, corrosion resistant properties of the biomimetic Ca–P coating were identified and their coating formation evolution as a function of hydrothermal time was established.

2. Experimental

2.1. Materials and chemicals

Employed as-extruded AZ31 alloy (Al 2.5–3.0, Zn 0.7–1.3, Mn > 0.20 and the balance Mg) was supplied by the Shandong Yin Guang Yu Yuan Light Metal Precision Molding Co., Ltd., China. PEI (99%, MW = 600), PAA (98%, MW = 800–1000) and PVP (95%, MW = 40,000) were purchased from Qingdao Jingke Chemical Reagent Co., Ltd., China. The substrates were cut into squares with dimension of 20 mm × 20 mm × 5 mm and were ground with SiC sand papers that were up to a 2500 grit. Then, they were cleaned with deionized (DI) water and alcohol solution and dried using warm air.

2.2. Coating preparation

The polished substrates were immersed in a 1 M NaOH solution at 60 °C for 1 h, followed by thoroughly cleaning with DI water and drying with warm air. Then, the LbL assembled templates were generated via a dip-coating method in the following sequence: "ABCBCBCBCBCB". Solutions A and C were consisted of the cationic polyelectrolytes PEI (pH 10.9) and PVP (pH 3.5) at concentrations of 10 and 5 g L^{-1} in DI water, respectively. Solution B contained the anionic polyelectrolyte PAA (pH 7.0) at a concentration of 10 g L^{-1} in DI water. The AZ31 substrates were incubated into solution A for 30 min and solution B and C for 5 min each. Five cycles were performed to obtain (PVP/PAA)$_5$ coated samples [35], and an additional PAA layer was set as the outermost layer.

The Ca–P coatings were prepared by hydrothermal treatment. Ca–P solution was prepared as calcium and phosphate precursors separately, and then mixed with the final concentration of 14 mM calcium nitrate ($Ca(NO_3)_2{\cdot}4H_2O$, ≥ 99.0%), 8.4 mM sodium dihydrogen phosphate ($NaH_2PO_4{\cdot}2H_2O$, ≥ 99.0%) and 4 mM sodium bicarbonate ($NaHCO_3$, ≥99.5%). $NaHCO_3$ was added to the phosphate solution as a buffering agent. The (PVP/PAA)$_{5.5}$ modified AZ31 substrate and the prepared Ca–P solution (60 mL) were transferred into 100 mL Teflon-lined 304 stainless steel reactors, which were maintained in an electric oven (DHG-9070 A, China) at 90 °C for 4 h. Finally, the samples were removed, washed thoroughly with DI water at least three times, and dried in electric oven at 80 °C (Called as II coating). A Ca–P solution containing PVP and PAA with the same concentration as LbL monomer solution (Called as III coating) and a sample without pretreated polyelectrolyte template (Called as I coating) were used as controls. The preparation process is schematically illustrated in Fig. 1.

2.3. Surface analysis

Field-emission scanning electron microscopy (FE-SEM, Nova NanoSEM 450, USA) was used to study the surface morphologies of the coatings. The possible chemical bonding formed in the coatings was confirmed by virtue of a Fourier transform infrared (FTIR) spectrophotometer (Nicolet 380, Thermo Electron Corporation, USA). X-ray diffractometer (XRD, Rigaku D/MAX 2500 PC, Japan) was employed to determine the crystal structures of the samples.

2.4. Corrosion characterization

2.4.1. Electrochemical test

An electrochemical analyzer (PAR Model 2273, Princeton, USA) was used to obtain the potentiodynamic polarization curves and electrochemical impedance spectra (EIS). A three-electrode cell set-up was selected in which the prepared sample with an exposed area of 1 cm^2 was the working electrode; and a saturated calomel electrode and a platinum sheet were acted as the reference and counter electrodes, respectively. A stable open circuit potential (OCP) was established with 600 s prior to the EIS testing. EIS studies were conducted at OCP for a

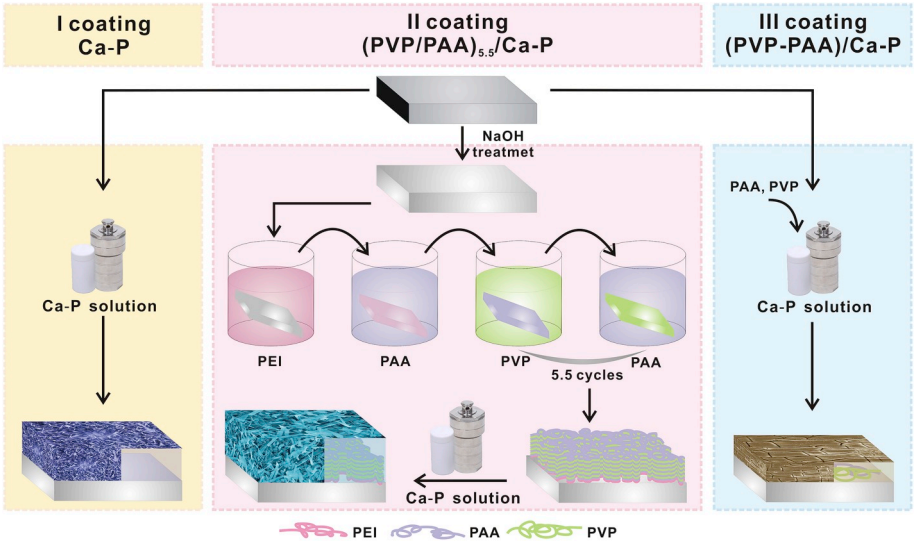

Fig. 1. Schematic construction of the Ca–P coatings via hydrothermal treatment.

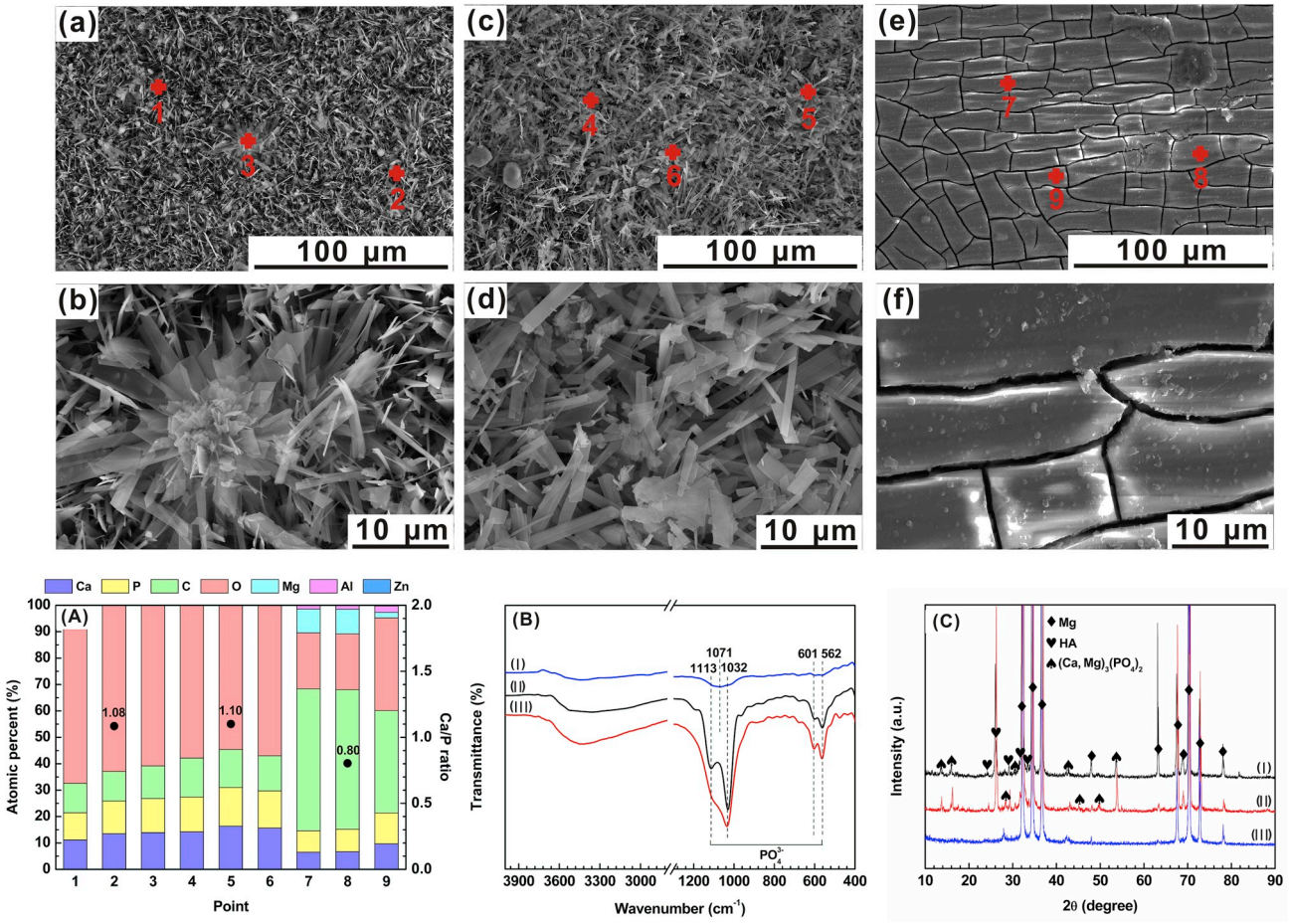

Fig. 2. SEM images of the (a and b) I, (c and d) II and (e and f) III coatings; (A) Element contents and corresponding Ca/P ratios, (B) FTIR spectra and (C) XRD patterns of the obtained coatings.

10-mV sinusoidal amplitude over a frequency range of 0.01 Hz–100 kHz. The acquired EIS plots were analyzed using ZSimpWin software (Version 3.10, USA) and best-fitted to the appropriate equivalent circuit (EC) models. After that, polarization of the samples started from approximately −2 V to −1 V with a scan rate of 1 mV s^{-1}. The obtained electrochemical parameters (corrosion potential (E_{corr}), corrosion current density (i_{corr}) and Tafel slopes (β_a and β_c)) were fitted using the Tafel extrapolation method. The experiment was performed in a corrosive environment of Hank's solution (8.0 g L^{-1} NaCl, 0.4 g L^{-1} KCl, 0.14 g L^{-1} $CaCl_2$, 0.35 g L^{-1} $NaHCO_3$, 1.0 g L^{-1} glucose ($C_6H_6O_6$), 0.1 g L^{-1} $MgCl_2{\cdot}6H_2O$, 0.06 g L^{-1} $MgSO_4{\cdot}7H_2O$, 0.06 g L^{-1} KH_2PO_4, and 0.06 g L^{-1} $Na_2HPO_4{\cdot}12H_2O$). The polarization resistance (R_p) and

corrosion protection efficiency (η) were calculated using Equations (1) and (2) [39–41]. All the electrochemical tests were repeated in triplicate to maintain the reproducibility.

$$R_p = \frac{\beta_a \cdot \beta_c}{2.303 i_{corr}(\beta_a + \beta_c)} \quad (1)$$

$$\eta = (i_{corr\ (bare)} - i_{corr\ (coated)}) / i_{corr\ (bare)} \times 100\% \quad (2)$$

where $i_{corr\ (bare)}$ and $i_{corr\ (coated)}$ represent the corrosion current density of bare AZ31 alloy and coated samples.

2.4.2. Hydrogen evolution test

Hydrogen evolution process was monitored by placing the substrates in Hank's solution at 37 °C under an inverted funnel connected to a graduated burette and testing the water level in the burette intermittently for 250 h with full surface exposure. Four samples for each condition were conducted to ensure the repeatability.

2.5. Scratch measurement

Scratch measurements were implemented to represent the adhesion force of the coating (critical load) via MML Nanotest system (Micro Materials, Ltd). Scratches of 2 mm length were made by a diamond Rockwell indenter with a spherical tip radius of 25 μm sliding at a constant speed of 2 mm min^{-1} under increasing loads from 0 to 20 N. Scratch images were captured using an in-situ optical microscope system in order to locate initial failure of the coating. The tests were repeated for three times.

3. Results

3.1. Surface analysis

Fig. 2 shows the SEM morphologies of the obtained three coatings under different conditions. For the I coating, it exhibits a stereoscopic blade morphology with some clusters (Fig. 2a and b). When the $(PVP/PAA)_{5.5}$ template is used, the coating becomes more compact than I coating (Fig. 2c and d). While for the III coating, it is obvious that the same concentration of free PVP and PAA in the Ca–P solution leads to many micro-cracks with a width of ~1 μm on the surface of the coating, and the coating displays an amorphous state (Fig. 2e and f).

The element contents and corresponding Ca/P ratios of the obtained coatings are displayed in Fig. 2A. The obtained three coatings are mainly composed of Ca, P, C and O elements. While for the III coating, some Mg, Al and Zn elements are found, which can be ascribed to the corrosion of the samples. The corresponding Ca/P ratios for the I, II, and III coatings are 1.08, 1.10 and 0.80. Fig. 2B and C shows the FTIR spectra and XRD patterns of the obtained three coatings, respectively. The peaks observed at 1113, 1071, 1032 cm^{-1} can be correlated to the ν_3 phosphate (PO_4^{3-}) region of HA. The doublet peaks at 601 and 562 cm^{-1} result from the ν_4 bending vibration of PO_4^{3-} [25,42]. The results are further confirmed in the XRD patterns (Fig. 2C). As expected, all the samples exhibit some high intense peaks corresponding to α-Mg, which may be ascribed to that the porous nature of the coatings [43]. The main composition of the obtained I and II coatings is HA and $(Ca, Mg)_3(PO_4)_2$, and the peaks intensity of II coating is much higher than the I coating. Only $(Ca, Mg)_3(PO_4)_2$ can be found on the surface of the III coating, which may be ascribed to the PVP and PAA in the Ca–P solution is not conducive to nucleation and growth of Ca–P crystals (Fig. 2) [37].

The cross-sectional images of I and II coatings are shown in Fig. 3. Both coatings display a similar morphology with different thickness, and the coatings can be divided into three layers. The whole thickness of I and II coatings is 6.91 and 12.69 μm, respectively. It is obvious that the inner two layers are more compact than the outer layer. From the EDS mapping images, the O content in the inner layer is higher than the outer layer, while the Ca and P contents in the inner layer is slightly lower than the outer layer, demonstrating that Mg may react with the Ca–P solution in the initial of the film formation.

The comparison between the scratched I and II coated samples is depicted in Fig. 4. Scratch damage starts with cracks emerged at the coating surface. The I and II coatings exhibit cracking and chipping at 9.94 and 10.69 N, respectively. The better adhesion of the II coating may be ascribed to the LbL assembled polyelectrolyte template, which can be coordinated with Ca^{2+} and PO_4^{3-} ions during the film formation. Yang et al. [44] showed that the critical load of micro arc oxidation ceramic coating on AZ31 substrates was about 13 N, which is higher than the obtained II coating. But the critical load of 10.69 N for the II coating is much higher than the $CaHPO_4{\cdot}2H_2O$ coating of 1.35 N on ZnAM50 sample [45] and the $(CIP/PAH)_{10}$/CIP induced HA coating of 2.70 N on AZ31 substrate [33].

3.2. Formation process

SEM morphologies (Fig. 5) with different hydrothermal times disclose the formation process of the II coating. In the initial of 10 min, some pores and cracks appear on the surface of the sample (Fig. 5a and b). After hydrothermal treatment with 30 min, a thin Ca–P coating with small flower-like crystals is preferentially deposited on the scratches (Fig. 5c and d), then the crystals grow up and cover the entire surface. After a 2-h hydrothermal treatment, the Ca–P coating is overlaid on the surface of the AZ31 alloy homogeneously (Fig. 5g and h). Then, the Ca–P coating becomes more and more compact after hydrothermal treatment of 3 h (Fig. 5i and j). The changes of compositions will be analyzed in Fig. 6.

Fig. 6 displays the (A) element contents and corresponding Ca/P ratios, (B) FTIR spectra and (C) XRD patterns of the II coating in the process of formation. It can be seen that the contents of Ca and P elements and Ca/P ratios increase with the hydrothermal time, and 2 h for the hydrothermal treatment later, the Ca and P elemental contents achieve a balance between the deposition and degradation of Ca–P crystal. The intensity of the peaks in FTIR spectra and XRD patterns also confirms the results in Fig. 6A. During the hydrothermal treatment, the main composition changes from $H_2PO_4^-$ at 1132, 1062 and 528 cm^{-1} ($Mg(H_2PO_4)_2$) to PO_4^{3-} at 1102, 1028, 600 and 561 cm^{-1} (HA and $(Ca, Mg)_3(PO_4)_2$), which also can be confirmed by the lower Ca and higher Mg contents in the inner layer of the cross-sectional images for the II coating (Fig. 3).

3.3. Corrosion behavior

Transient thermodynamic and kinetic information on the electrochemical corrosion of all the samples in Hank's solution is provided by the potentiodynamic polarization curves in Fig. 7. The corresponding parameters of all the samples are listed in Table 1. All the coated samples show lower i_{corr} values compared with the bare AZ31 samples, and the II coating (8.05×10^{-8} A cm^{-2}) exhibits the lowest i_{corr} values among all the coated samples. This value is nearly three orders of magnitude lower than those of the bare AZ31 (1.96×10^{-5} A cm^{-2}). In addition, the polarization curves of the different samples show differences in both the anodic and cathodic polarization regions. The bare AZ31 displays typical active anodic polarization curves, with a steady increase of the Mg dissolution rate for all the anodic part, indicating that the surface of AZ31 substrate possesses a high active state. In contrast, all coated samples show a noticeable passivation-like section in the anodic polarization, revealing the suppressed anodic dissolution reaction as the rate-determining step. Note that, the cathodic hydrogen evolution reaction is also restrained in all the coated Mg samples, which can be confirmed in Fig. 9. The II coating processes the highest R_p and η values, demonstrating the good corrosion resistance of the induced Ca–P coating.

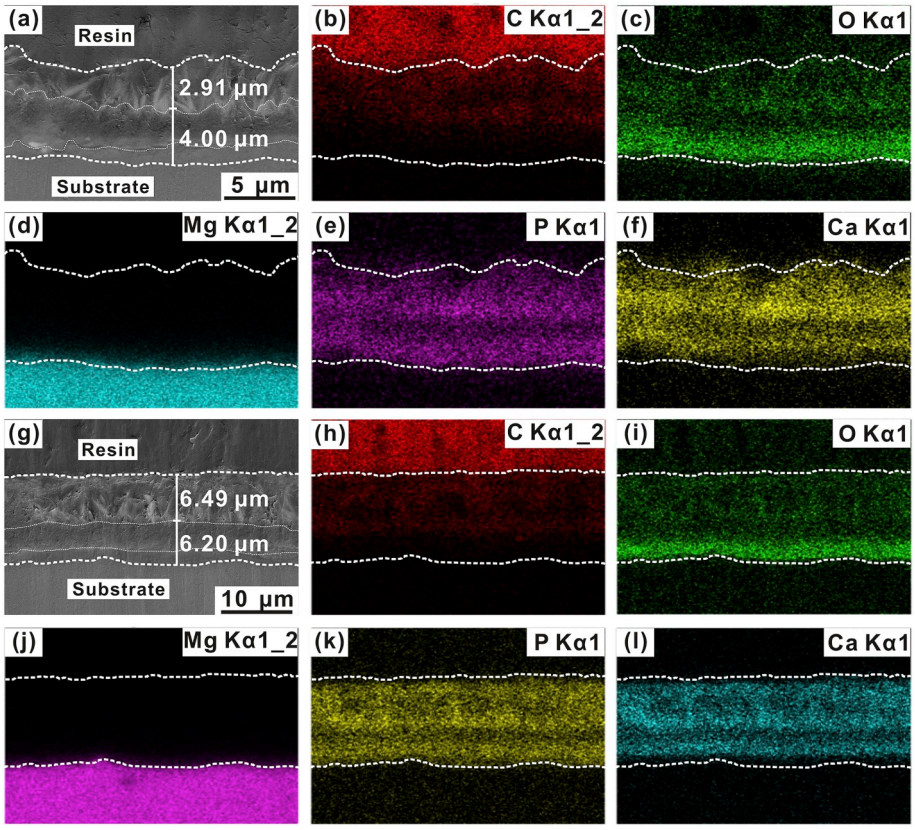

Fig. 3. Cross-sectional images and corresponding EDS mapping of the (a–f) I and (g–l) II coatings.

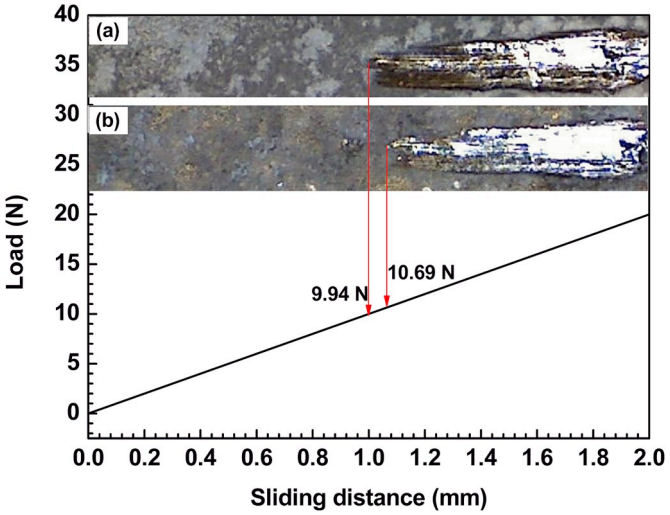

Fig. 4. Scratch track view of the bare AZ31 in comparison to (a) I and (b) II coatings.

The corrosion mechanisms of the samples are further evaluated by EIS curves, which are shown in Fig. 8 with the corresponding EC models. The diameters of the capacitive loops for all samples can be ranked as follows: II coating > III coating > I coating > AZ31 substrate. Generally speaking, the larger capacitive loop represents the better corrosion resistance, implying that the Ca–P coating, induced by LbL assembled template, has the best protection against corrosive ions in Hank's solution.

The Nyquist plots (Fig. 8A–C) display that the bare and coated AZ31 are characterized by two and three capacitive loops in the different ranges of frequency, respectively. For the bare AZ31, CPE_1 and R_{f1} are used to characterize the corrosion products layer in the high-frequency range. The low-frequency capacitive loop is described by CPE_2 and R_{ct} to characterize the interfacial charge transfer reaction. Differently, three capacitive loops are related to the three Ca–P coatings, which have a dense inner layer and a loose outer layer (Fig. 3), represented with R_{f1} and R_{f2} in collocation with CPE_1 and CPE_2 [46]. In both ECs, R_s, R_f and R_{ct} represent the solution resistance, coating resistance and charge transfer resistance. A constant phase element (*CPE*) is used instead of a pure capacitive, which is defined by admittance (Y_0) and power index number (n), and can be calculated by the formula of $Y_{CPE}(\omega) = 1/Z_{CPE} = Y_0(j\omega)^n$ [27]. The fitting results of EIS data are listed in Table 2. The highest R_{ct} values of II coating also confirms the good corrosion protection to hinder the permeation of the corrosive ions.

Bode plots of Fig. 8D show that the impedance modulus of Ca–P coated samples are higher than that of the bare AZ31. The II coating has an impedance modulus of $1.7 \times 10^5\ \Omega\ cm^2$, which is higher than the III coating of $6.4 \times 10^4\ \Omega\ cm^2$ and I coating of $1.2 \times 10^4\ \Omega\ cm^2$. The phase angles (Fig. 8E) of II and III coatings with three time constants are higher than the I coating and bare AZ31. The phase angle of I coating is close to 46°, lower than that of the other specimens, which may be caused by the incompactness of the coating. But it has a wider range of frequencies with an additional time constant than the untreated AZ31 [20]. These reveal that the II coating is an effective physical barrier to corrosion in Hank's solution.

Hydrogen evolution volume (HEV) and rate (HER) for the four samples are used to evaluate the corrosion behavior during a 250-h immersion in Hank's solution (Fig. 9). It is obvious that the II coating has the lowest HEV and HER over an entire period of immersion time. The HEV and HER for I coating are slightly lower than the bare AZ31, attributing to the corrosion protection of Ca–P coating. For the III coating, the HEV and HER are lower than that of the I coating in stage I, demonstrating that the corrosion resistance of the III coating is better than the I coating in the short term, which is consistent with

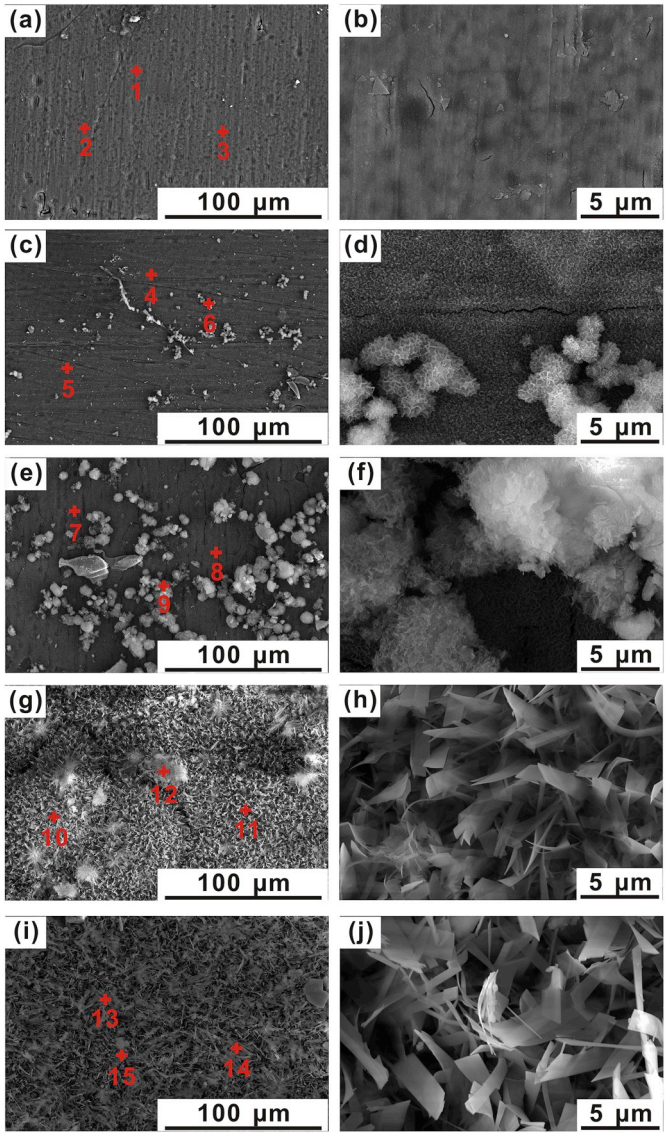

Fig. 5. SEM images of the II coating in the process of formation: (a and b) 10 min, (c and d) 30 min, (e and f) 1 h, (g and h) 2 h and (i and j) 3 h.

electrochemical results in Figs. 7 and 8. After then, the HEV and HER of the III coating increase gradually until they are higher than the I coating (stage II) and AZ31 substrate (stage III), which may be ascribed to a large number of microcracks in the coating acted as the invasion channels for corrosive ions, accelerating galvanic corrosion of the AZ31

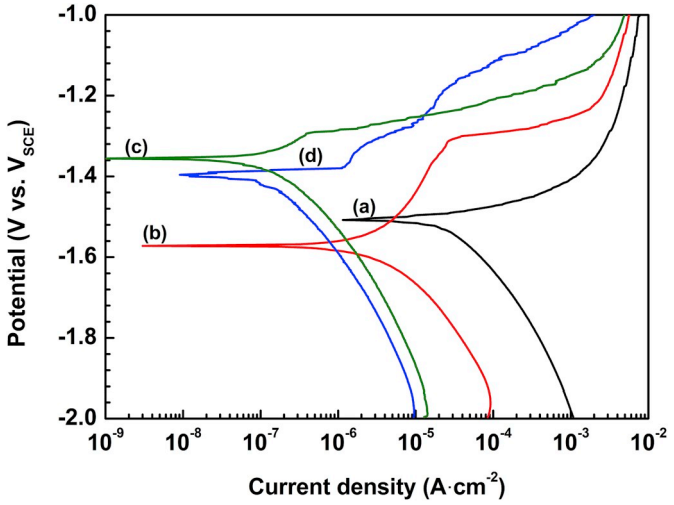

Fig. 7. Potentiodynamic polarization curves of the (a) AZ31 substrate, (b) I, (c) III and (d) II coatings in Hank's solution.

substrate (Fig. 2). In the initial 15 h, the HERs for all samples decrease due to the formation of $Mg(OH)_2$ corrosion product. After an immersion of 250 h, the corrosion rates of four samples can be ranked as: III coating (0.0102 ± 0.0022 mL cm^{-2} h^{-1}) > AZ31 substrate (0.0089 ± 0.0042 mL cm^{-2} h^{-1}) > I coating (0.0110 ± 0.0015 mL cm^{-2} h^{-1}) > II coating (0.0056 ± 0.0054 mL cm^{-2} h^{-1}). The photographs of the four samples after an immersion of 250 h are shown in Fig. 9C, a complete and dense coating is still presented on the surface of the AZ31 substrate for II coating, agreeing with the results of the hydrogen evolution test. Thus, II coating exhibits the best corrosion protection during immersed in Hank's solution for 250 h.

SEM images of the AZ31 substrate, I and II coatings after an immersion of 250 h in Hank's solution are displayed in Fig. 10a-f. Many cracks of corrosion products with a width of ~5 μm appear on the surface of the bare AZ31. While for the I coating, the distribution of the lamellar structure is uneven with some cluster of blocks, due to the precipitation of the corrosion products. It is no obvious changes for the II coating, confirming the good corrosion resistance during immersion. FTIR spectra and XRD patterns of the samples after an immersion of 250 h in Hank's solution are shown in Fig. 10A and B. The peaks observed at 1106, 1063 and 1029 cm^{-1} can be correlated to the ν_3 phosphate (PO_4^{3-}) region of HA. The doublet peaks at 600 and 562 cm^{-1} result from the ν_4 bending vibration of PO_4^{3-} [25,42]. The peaks appeared at 1374 and 868 cm^{-1} are related to the vibration of HPO_4^{2-} [42]. And the peak presented at 1433 cm^{-1} results from ν_3 vibration of CO_3^{2-} [25]. These results will be further confirmed in the XRD patterns (Fig. 10B). The main composition of the obtained I and II coatings remains to be HA and (Ca, Mg)$_3$(PO$_4$)$_2$, and (Ca, Mg)$_3$(PO$_4$)$_2$

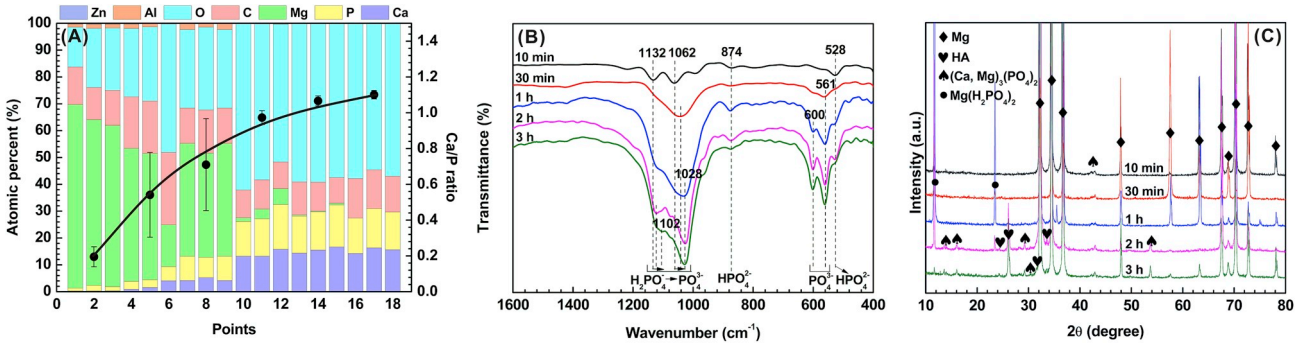

Fig. 6. (A) Element contents and corresponding Ca/P ratios (Pointed in Figs. 5 and 2), (B) FTIR spectra and (C) XRD patterns of the II coating in the process of formation.

Table 1
Electrochemical parameters of the polarization curves for the bare and coated AZ31 in Hank's solution.

Samples	E_{corr} (V)	i_{corr} (A·cm^{-2})	β_a (mV·dec^{-1})	-β_c (mV·dec^{-1})	R_p (Ω·cm^2)	η (%)
AZ31	−1.51	1.96 × 10^{-5}	47.12	170.97	1.60 × 10^6	
I coating	−1.57	1.77 × 10^{-6}	147.26	116.74	1.59 × 10^7	90.97
II coating	−1.36	8.05 × 10^{-8}	115.38	168.60	3.69 × 10^8	99.59
III coating	−1.40	1.07 × 10^{-7}	66.88	155.06	1.90 × 10^8	99.45

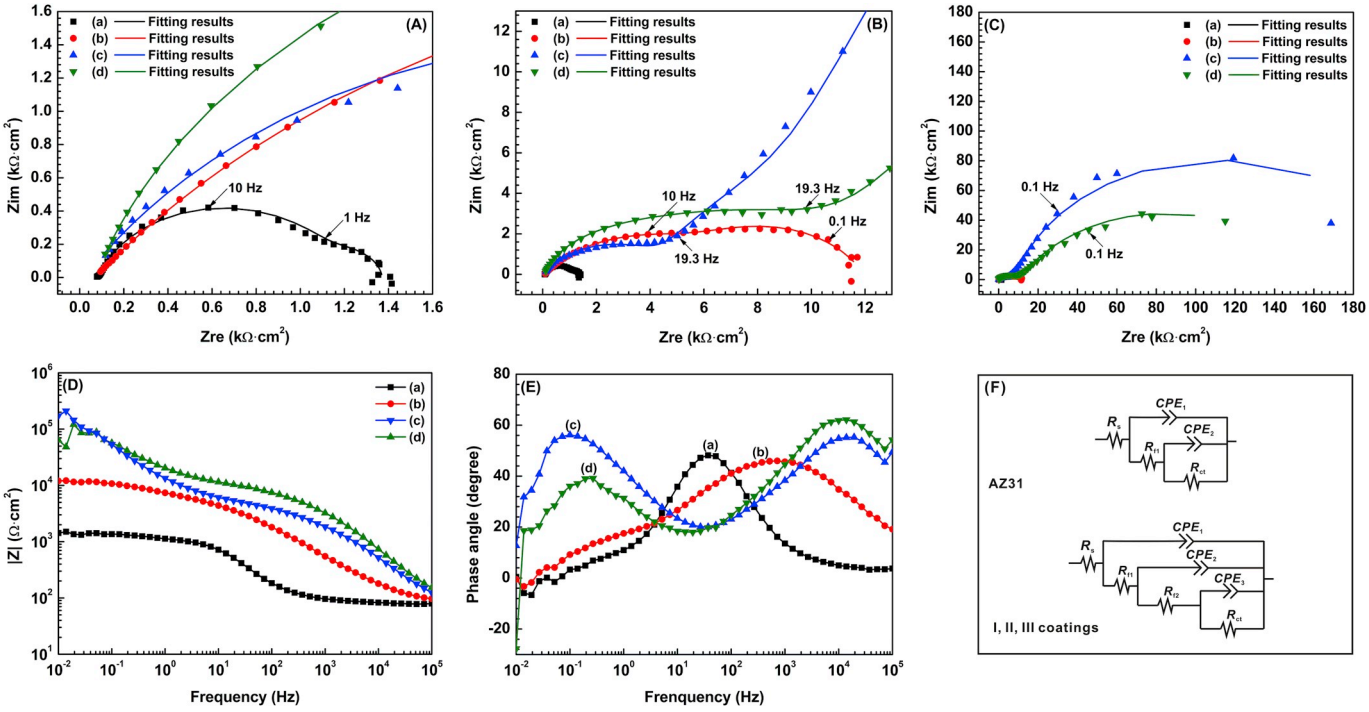

Fig. 8. (A–C) Nyquist, (D and E) Bode plots and (F) corresponding EC models of the (a) AZ31 substrate, (b) I, (c) II and (d) III coatings in Hank's solution.

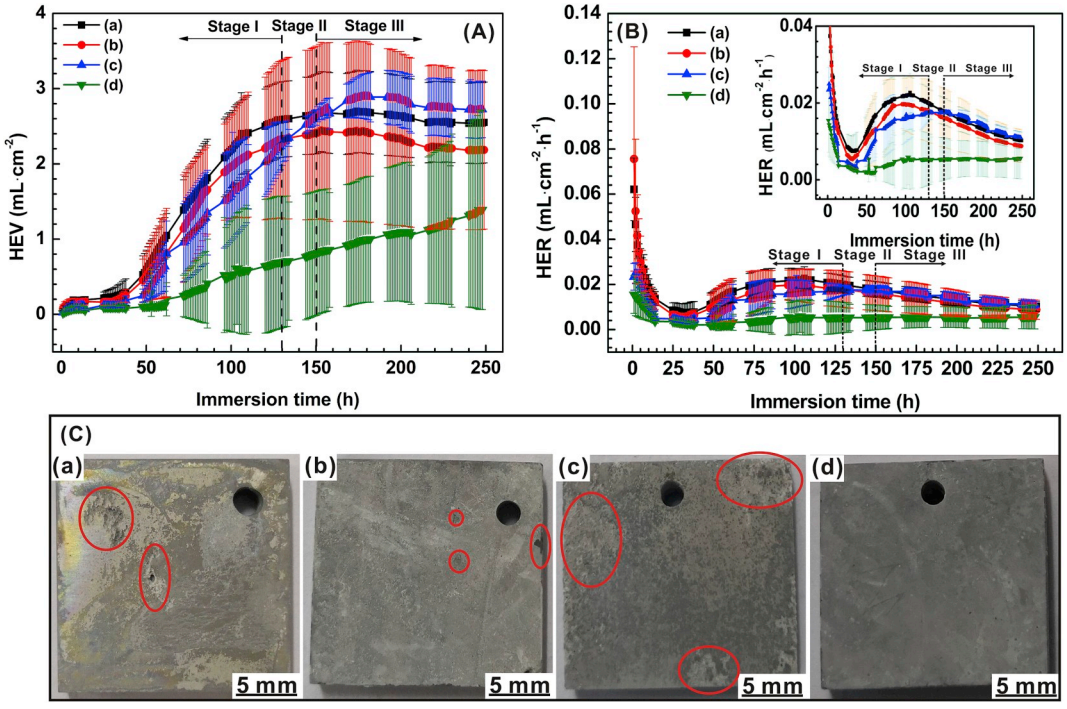

Fig. 9. (A) HEV, (B) HER curves and (C) photographs with an immersion of 250 h: (a) AZ31 substrate, (b) I, (c) III and (d) II coatings in Hank's solution.

Table 2
Electrochemical data obtained by equivalent circuit fitting of EIS curves for all samples.

Samples	R_s ($\Omega \cdot cm^2$)	CPE_1 ($\Omega^{-1} \cdot s^n \cdot cm^{-2}$)	n_1	R_{f1} ($\Omega \cdot cm^2$)	CPE_2 ($\Omega^{-1} \cdot s^n \cdot cm^{-2}$)	n_2	R_{f2} ($\Omega \cdot cm^2$)	CPE_3 ($\Omega^{-1} \cdot s^n \cdot cm^{-2}$)	n_3	R_{ct} ($\Omega \cdot cm^2$)	*chi*
AZ31	82.66	3.79×10^{-5}	0.81	1136	2.73×10^{-3}	1.00				1.55×10^{2}	2.11×10^{-3}
I coating	69.26	9.74×10^{-6}	0.60	4987	4.32×10^{-5}	0.95	2.51×10^{3}	2.52×10^{-4}	1.00	2.02×10^{3}	7.50×10^{-4}
II coating	60.02	1.25×10^{-6}	0.66	7187	1.22×10^{-5}	0.80	1.36×10^{4}	1.40×10^{-5}	0.89	1.99×10^{5}	5.11×10^{-3}
III coating	71.26	1.56×10^{-7}	0.82	5171	3.31×10^{-6}	0.61	7.65×10^{3}	1.83×10^{-5}	0.70	1.47×10^{5}	5.07×10^{-3}

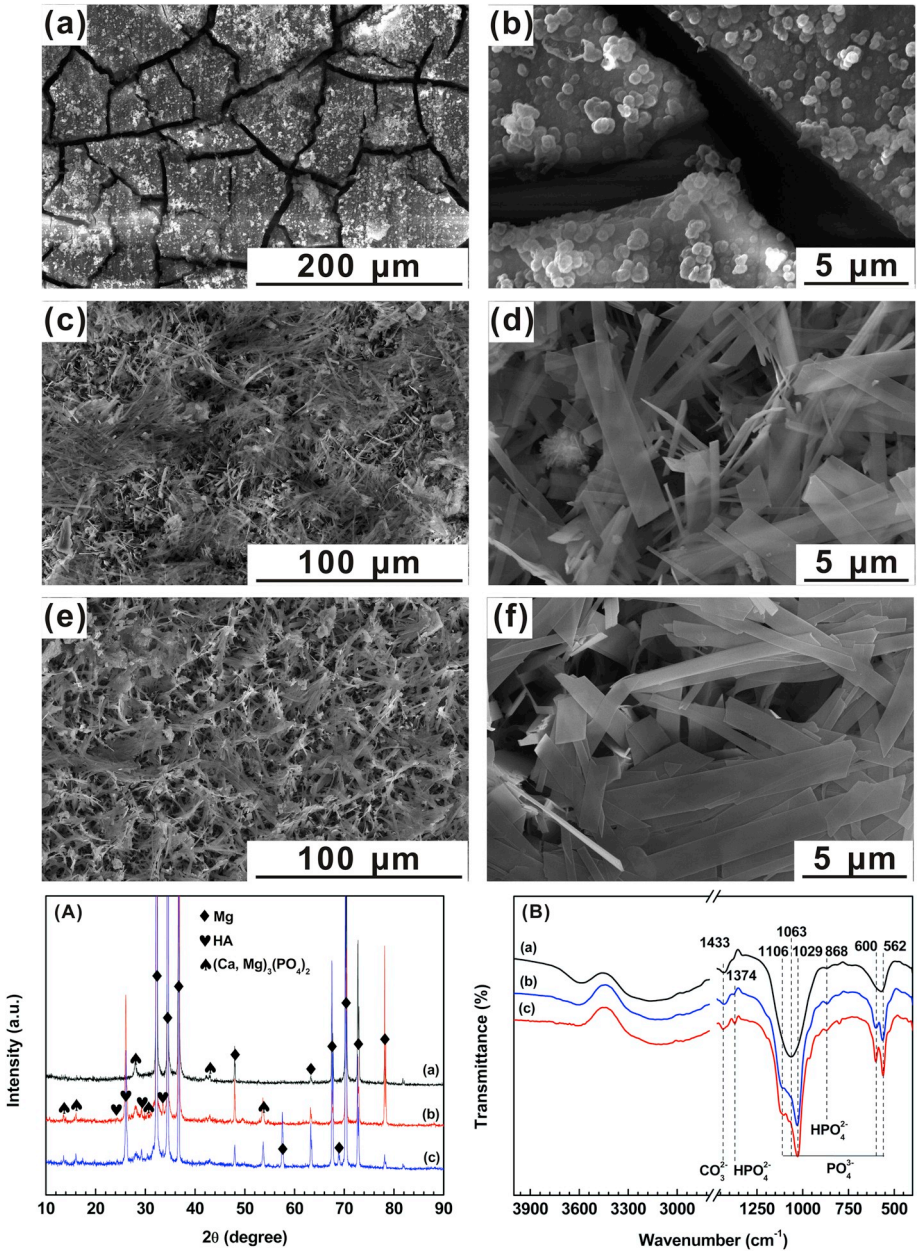

Fig. 10. SEM images of the (a and b) AZ31 substrate, (c and d) I and (e and f) II coatings after an immersion of 250 h in Hank's solution, and (A) FTIR spectra and (B) XRD patterns of the (a) AZ31 substrate, (b) I and (c) II coatings after an immersion of 250 h in Hank's solution.

precipitate is observed on the surface of the AZ31 substrate after 250 h immersion. The stability morphology and composition of the coatings also indicate the good corrosion resistance of the II coating during immersion.

4. Discussion

4.1. Influence of the coating preparation methods and inducers

In general, the preparation method is a primary factor to affect the properties of Ca–P coatings. It is obvious that the Ca–P coating formed by HDP [38] provides best corrosion resistance among all coating

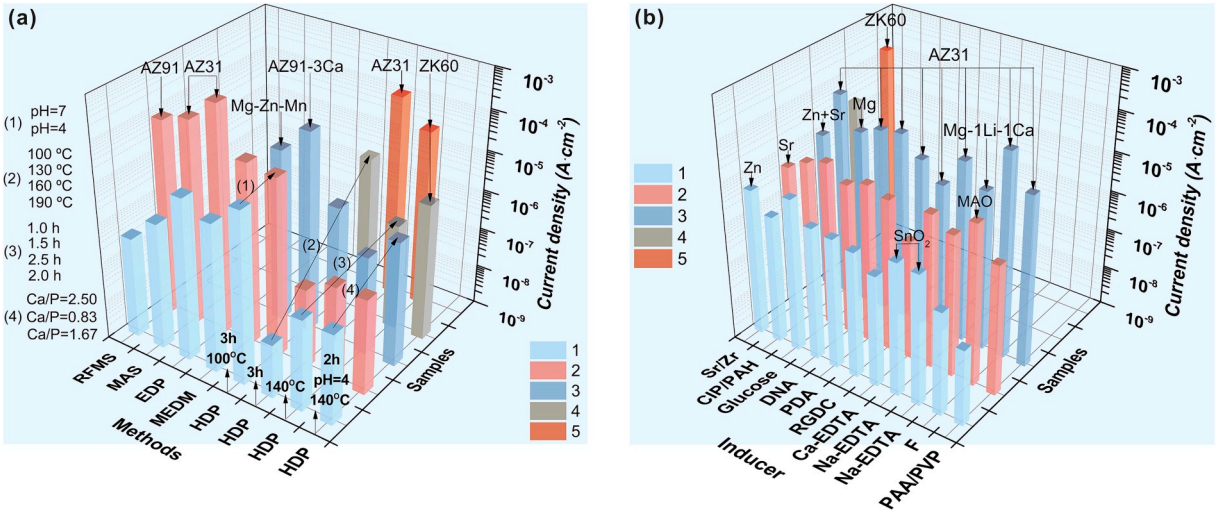

Fig. 11. Current densities of the Ca–P coatings (a) formed by different methods and conditions [14,19,38,47–51], and (b) formed with different inducers [10,11,18,20,26,29,33,52–54].

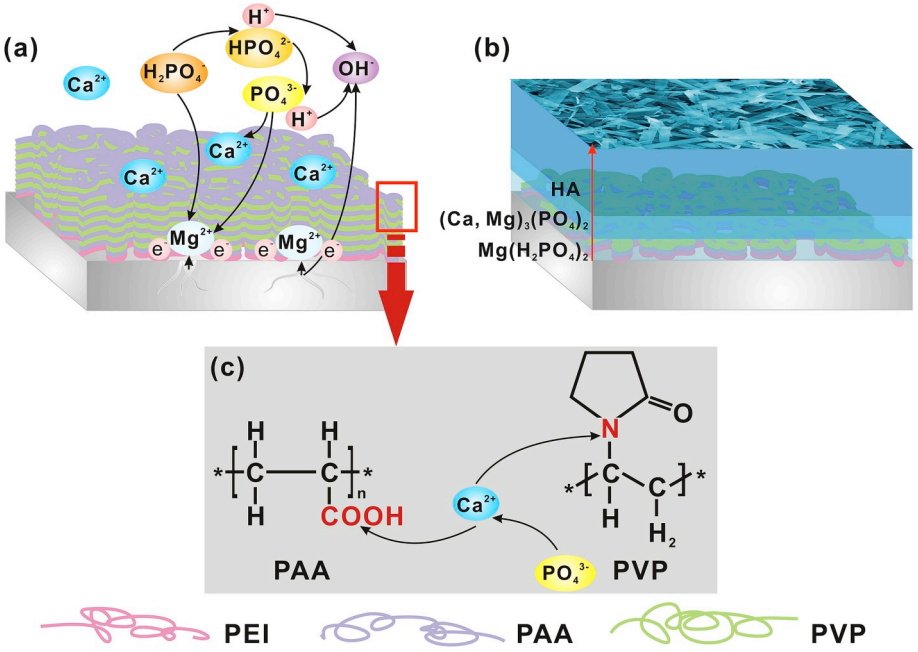

Fig. 12. Schematic coating formation mechanism of the II coating via hydrothermal treatment with LbL assembled templates.

preparation methods, such as radio frequency magnetron sputtering [47], microwave aqueous synthesis (MAS) [48], EDP [49] and mixed electric discharge machining (MEDM) [14]. For the HDP method, the different pH value [19] and Ca/P ratio [50] of the hydrothermal solution, hydrothermal temperature [38] and time [51] and types of alloy lead to the different Ca–P coating with different properties. Thus, the HDP becomes the most commonly used coating preparation method due to its simple operation and easy control of variables.

In order to improve the corrosion resistance of Mg alloys in further, many inducers are selected to construct the Ca–P coatings to improve its integrity and compactness. The i_{corr} of the Ca–P coatings formed with different inducer is exhibited in Fig. 11a. It can be seen that the Ca–P coatings with the organic inducers, especially for glucose [18], deoxyribonucleic acid (DNA) [52], PDA [26], RGDC [11], have a better improvement in corrosion resistance than the Ca–P coatings with the inorganic inducers [53,54]. Compared with the Na-EDTA [10,29], the Ca-EDTA [20] can be used to form a Ca–P coating with good corrosion resistance. Although the heterogeneous nucleation of SnO_2 is helpful for film formation, the enhancement of corrosion resistance is still limited. Otherwise, a LbL assembled $(CIP/PAH)_{10}$/CIP multilayer is also used to prepare a HA coating, but the increase of corrosion resistance is lesser than the $(PVP/PAA)_{5.5}$ induced Ca–P coating on AZ31 substrate [33]. This can be ascribed to the molecular structure of the assembly monomer, which is plenty of –COOH in PAA.

When the pH value of PAA solution is 7.0, the pKa of PAA solution is 6.64, thus the distribution fraction of -COO^- in PAA can be calculated with:

$$\delta_0 = 1 - \frac{[H^+]}{Ka + [H^+]} \quad (3)$$

Where δ_0 is the distribution fraction after one step dissociation, Ka is the acid equilibrium constant.

Thus, the distribution fraction of -COO^- in PAA is 0.6961, indicating most of the –COOH changes to -COO^-, which is beneficial to the adsorption of Ca^{2+} to develop Ca-PAA complex.

Kaabi Falahieh Asl et al. [55] has formed a Ca–P coating with PAA,

which the PAA is mixed in the phosphate and calcium ion precursors. The obtained Ca–P coating displays a good corrosion protection with good cytocompatibility, and the incorporation of PAA in the coating changes the phase formation route during HDP process. By increasing the PAA concentration, the formation of the tricalcium phosphate phase increases. But the coating shows a globular morphology with some pores, hindering the protection for Mg substrates due to the penetration of the corrosive ions. Therefore, a $(PVP/PAA)_{5.5}$ template is beneficial to prepare a more compact and homogeneous foliated Ca–P coating (Fig. 2) to protect the bare AZ31 for a long term (Fig. 9). As the similar compositions with natural bone, the obtained II coating good cytocompatibility may be suitable to be applied as orthopedic implants.

4.2. Coating formation mechanism

The coating formation mechanisms of the II coating via HDP with LbL assembled templates are shown in Fig. 12. In the initial stage of HDP, the water molecules are penetrated through the LbL assembled $(PVP/PAA)_{5.5}$ templates. The electrochemical corrosion of the skin layer for the AZ31 substrate results in some Mg^{2+} ions (Equations (4)–(6)).

$$Mg \rightarrow Mg^{2+} + 2e^{-} \quad (4)$$

$$2H_2O + 2e^{-} \rightarrow 2OH^{-} + H_2\uparrow \quad (5)$$

$$Mg + 2H_2O \rightarrow Mg(OH)_2 + H_2\uparrow \quad (6)$$

An inner $Mg(H_2PO_4)_2$ can be formed by:

$$Mg^{2+} + 2H_2PO_4^{-} \rightarrow Mg(H_2PO_4)_2 \quad (7)$$

Stereoscopic blade-shaped Ca–P coating is formed on the surface of the AZ31 substrate, which is a typical result of the strong electrostatic interaction between the $-COO^{-}$ groups (PAA) or polar lactam bonds (PVP) and Ca^{2+} ions. A $(PVP/PAA)_{5.5}$ template is beneficial to the homogeneous adsorption of Ca^{2+} ions, improving the nucleation and growth of the Ca–P coating.

Then, the dihydrogen phosphate ($H_2PO_4^{-}$) ions are transformed into phosphate (PO_4^{3-}) ions through the following ionic reactions (Equations (8) and (9)):

$$H_2PO_4^{-} + OH^{-} \rightarrow HPO_4^{2-} + H_2O \quad (8)$$

$$HPO_4^{2-} + OH^{-} \rightarrow PO_4^{3-} + H_2O \quad (9)$$

Thus, the Ca–P coating composed of $Mg(H_2PO_4)_2$, $(Ca, Mg)_3(PO_4)_2$ and HA is obtained by the following reactions:

$$3Ca^{2+} + 3Mg^{2+} + 2PO_4^{3-} \rightarrow (Ca, Mg)_3(PO_4)_2 \quad (10)$$

$$10Ca^{2+} + 2OH^{-} + 6PO_4^{3-} \rightarrow Ca_{10}(PO_4)_6(OH)_2 \quad (11)$$

However, the free PAA and PVP mixed in Ca–P solution may go against the nucleation and growth of the Ca–P crystals (Fig. 2) to the disadvantages of the corrosion protection for Mg alloys (Fig. 9).

5. Conclusion

A novel polyelectrolyte multilayer template, based on PAA and PVP via LbL assembly, is used to construct biomimetic Ca–P coating to improve the corrosion resistance of the AZ31 alloy.

(1) The polyelectrolyte multilayer induced Ca–P coating shows a compact stereoscopic blade morphology with the thickness of 12.69 μm.
(2) The $(PVP/PAA)_{5.5}$ template improves the binding force of the Ca–P coating from 9.94 to 10.69 N.
(3) Both hydrogen evolution and electrochemical corrosion tests demonstrated that the template-induced Ca–P coating exhibits a good corrosion protection for AZ31 alloy.
(4) The free PAA and PVP may go against the nucleation and growth of the Ca–P crystals, but the LbL assembled $(PVP/PAA)_{5.5}$ template, which the distribution fraction of $-COO^{-}$ in PAA is 0.6961, is beneficial to the formation of the crystalline Ca–P coating, because most of the –COOH changes to $-COO^{-}$ to adsorb Ca^{2+} for development of Ca-PAA complex.

CRediT authorship contribution statement

Lan-Yue Cui: Conceptualization, Formal analysis, Writing - original draft. **Shen-Cong Cheng:** Data curation. **Lu-Xian Liang:** Data curation. **Jing-Chao Zhang:** Data curation. **Shuo-Qi Li:** Funding acquisition. **Zhen-Lin Wang:** Data curation. **Rong-Chang Zeng:** Funding acquisition, Writing - review & editing.

Declaration of competing interest

The authors declared that they have no conflicts of interest to this work.

Acknowledgements

This work was supported by the National Natural Science Foundation of China (51571134), Shandong Provincial Natural Science Foundation (ZR2017BEM002), and Shandong University of Science and Technology Research Fund (2014TDJH104).

References

[1] Y. Liu, Y.F. Zheng, X.H. Chen, J.A. Yang, H.B. Pan, D.F. Chen, L.N. Wang, J.L. Zhang, D.H. Zhu, S.L. Wu, K.W.K. Yeung, R.C. Zeng, Y. Han, S.K. Guan, Fundamental theory of biodegradable metals-definition, criteria, and design, Adv. Funct. Mater. (2019) 1805402.
[2] L.C. Zhang, M. Xu, Y.D. Hu, F. Gao, T. Gong, T. Liu, X. Li, C.J. Pan, Biofunctionization of biodegradable magnesium alloy to improve the in vitro corrosion resistance and biocompatibility, Appl. Surf. Sci. 451 (2018) 20–31.
[3] X.J. Ji, L. Gao, J.C. Liu, J. Wang, Q. Cheng, J.P. Li, S.Q. Li, K.Q. Zhi, R.C. Zeng, Z.L. Wang, Corrosion resistance and antibacterial properties of hydroxyapatite coating induced by gentamicin-loaded polymeric multilayers on magnesium alloys, Colloids Surf., B 179 (2019) 429–436.
[4] Y. Pei, G. Zhang, C. Zhang, J. Wang, R. Hang, X. Yao, X. Zhang, Corrosion resistance, anticoagulant and antibacterial properties of surface-functionalized magnesium alloys, Mater. Lett. 234 (2019) 323–326.
[5] Y.B. Zhao, H.P. Liu, C.Y. Li, Y. Chen, S.Q. Li, R.C. Zeng, Z.L. Wang, Corrosion resistance and adhesion strength of a spin-assisted layer-by-layer assembled coating on AZ31 magnesium alloy, Appl. Surf. Sci. 434 (2018) 787–795.
[6] D.D. Xia, Y. Liu, S.Y. Wang, R.C. Zeng, Y.S. Liu, Y.F. Zheng, Y.S. Zhou, In vitro and in vivo investigation on biodegradable Mg-Li-Ca alloys for bone implant application, Sci. China Mater. (2018) 1–17.
[7] Y.B. Zhao, L.Q. Shi, X.J. Ji, J.C. Li, Z.Z. Han, S.Q. Li, R.C. Zeng, F. Zhang, Z.L. Wang, Corrosion resistance and antibacterial properties of polysiloxane modified layer-by-layer assembled self-healing coating on magnesium alloy, J. Colloid Interface Sci. 526 (2018) 43–50.
[8] D. Zhang, Z. Qi, H. Shen, B. Wei, Y. Zhang, Z. Wang, In vitro degradation and cytocompatibility of magnesium alloy coated with Hf/PLLA duplex coating, Mater. Lett. 213 (2018) 249–252.
[9] L.Y. Cui, X.H. Fang, W. Cao, R.C. Zeng, S.Q. Li, X.B. Chen, Y.H. Zou, S.K. Guan, E.H. Han, In vitro corrosion resistance of a layer-by-layer assembled DNA coating on magnesium alloy, Appl. Surf. Sci. 457 (2018) 49–58.
[10] L.Y. Cui, G.B. Wei, Z.Z. Han, R.C. Zeng, L. Wang, Y.H. Zou, S.Q. Li, D.K. Xu, S.K. Guan, In vitro corrosion resistance and antibacterial performance of novel tin dioxide-doped calcium phosphate coating on degradable Mg-1Li-1Ca alloy, J. Mater. Sci. Technol. 35 (2019) 254–265.
[11] L. Cao, L. Wang, L. Fan, W. Xiao, B. Lin, Y. Xu, J. Liang, B. Cao, RGDC peptide-induced biomimetic calcium phosphate coating formed on AZ31 magnesium alloy, Materials 10 (2017) 358.
[12] Y.B. Zhao, L.Q. Shi, L.Y. Cui, C.L. Zhang, S.Q. Li, R.C. Zeng, F. Zhang, Z.L. Wang, Corrosion resistance of silane-modified hydroxyapatite films on degradable magnesium alloys, Acta Metall. Sin. 31 (2018) 180–188.
[13] H. Wang, S. Zhu, L. Wang, Y. Feng, X. Ma, S. Guan, Formation mechanism of Ca-deficient hydroxyapatite coating on Mg-Zn-Ca alloy for orthopaedic implant, Appl. Surf. Sci. 307 (2014) 92–100.
[14] C. Prakash, S. Singh, B.S. Pabla, M.S. Uddin, Synthesis, characterization, corrosion and bioactivity investigation of nano-HA coating deposited on biodegradable Mg-Zn-Mn alloy, Surf. Coating. Technol. 346 (2018) 9–18.
[15] S. Mohajernia, S. Pour-Ali, S. Hejazi, M. Saremi, A.R. Kiani-Rashid, Hydroxyapatite coating containing multi-walled carbon nanotubes on AZ31 magnesium:

mechanical-electrochemical degradation in a physiological environment, Ceram. Int. 44 (2018) 8297–8305.
[16] A. Roy, S.S. Singh, M.K. Datta, B. Lee, J. Ohodnicki, P.N. Kumta, Novel sol-gel derived calcium phosphate coatings on Mg4Y alloy, Mater. Sci. Eng., B 176 (2011) 1679–1689.
[17] M. Ren, S. Cai, G. Xu, X. Ye, Y. Dou, K. Huang, X. Wang, Influence of heat treatment on crystallization and corrosion behavior of calcium phosphate glass coated AZ31 magnesium alloy by sol-gel method, J. Non-Cryst. Solids 369 (2013) 69–75.
[18] L.Y. Li, L.Y. Cui, B. Liu, R.C. Zeng, X.B. Chen, S.Q. Li, Z.L. Wang, E.H. Han, Corrosion resistance of glucose-induced hydrothermal calcium phosphate coating on pure magnesium, Appl. Surf. Sci. 465 (2019) 1066–1077.
[19] A. Ali, F. Iqbal, A. Ahmad, F. Ikram, A. Nawaz, A.A. Chaudhry, S.A. Siddiqi, I. Rehman, Hydrothermal deposition of high strength calcium phosphate coatings on magnesium alloy for biomedical applications, Surf. Coating. Technol. 357 (2019) 716–727.
[20] Z. Chunyan, Z. Shiyu, L. Xinpeng, H. Hongchuan, Microstructure and corrosion properties of calcium phosphate coating on magnesium alloy prepared by hydrothermal treatment at various pH values, Rare Met. Mater. Eng. 47 (2018) 2993–2999.
[21] S.V. Dorozhkin, Calcium orthophosphate coatings on magnesium and its biodegradable alloys, Acta Biomater. 10 (2014) 2919–2934.
[22] Q. He, Z. Huang, Controlled synthesis and morphological evolution of dendritic porous microspheres of calcium phosphates, J. Porous Mater. 16 (2008) 683–689.
[23] S. Hiromoto, Self-healing property of hydroxyapatite and octacalcium phosphate coatings on pure magnesium and magnesium alloy, Corrosion Sci. 100 (2015) 284–294.
[24] N. Ohtsu, S. Hiromoto, M. Yamane, K. Satoh, M. Tomozawa, Chemical and crystallographic characterizations of hydroxyapatite and octacalcium phosphate-coatings on magnesium synthesized by chemical solution deposition using XPS and XRD, Surf. Coating. Technol. 218 (2013) 114–118.
[25] W. Cui, E. Beniash, E. Gawalt, Z. Xu, C. Sfeir, Biomimetic coating of magnesium alloy for enhanced corrosion resistance and calcium phosphate deposition, Acta Biomater. 9 (2013) 8650–8659.
[26] B. Lin, M. Zhong, C. Zheng, L. Cao, D. Wang, L. Wang, J. Liang, B. Cao, Preparation and characterization of dopamine-induced biomimetic hydroxyapatite coatings on the AZ31 magnesium alloy, Surf. Coating. Technol. 281 (2015) 82–88.
[27] Y. Guo, S. Jia, L. Qiao, Y. Su, R. Gu, G. Li, J. Lian, Enhanced corrosion resistance and biocompatibility of polydopamine/dicalcium phosphate dihydrate/collagen composite coating on magnesium alloy for orthopedic applications, J. Alloys Compd. (2019) 152782, https://doi.org/10.1016/j.jallcom.2019.152782.
[28] P. Xiong, Z. Jia, M. Li, W. Zhou, J. Yan, Y. Wu, Y. Cheng, Y. Zheng, Biomimetic Ca, Sr/P-doped silk fibroin films on Mg-1Ca alloy with dramatic corrosion resistance and osteogenic activities, ACS Biomater. Sci. Eng. 4 (2018) 3163–3176.
[29] L.Y. Cui, G.B. Wei, R.C. Zeng, S.Q. Li, Y.H. Zou, E.H. Han, Corrosion resistance of a novel SnO_2-doped dicalcium phosphate coating on AZ31 magnesium alloy, Bioact. Mater. 3 (2018) 245–249.
[30] K. Abdelkebir, S. Morin-Grognet, F. Gaudiere, G. Coquerel, B. Labat, H. Atmani, G. Ladam, Biomimetic layer-by-layer templates for calcium phosphate biomineralization, Acta Biomater. 8 (2012) 3419–3428.
[31] P.A. Ngankam, Influence of polyelectrolyte multilayer films on calcium phosphate nucleation, J. Am. Chem. Soc. 122 (2000) 8998–9005.
[32] X.R. Li, J.W. Xie, X.Y. Yuan, Y.N. Xia, Coating electrospun poly(ε-caprolactone) fibers with gelatin and calcium phosphate and their use as biomimetic scaffolds for bone tissue engineering, Langmuir 24 (2008) 14145–14150.
[33] X.J. Ji, L. Gao, J.C. Liu, R.Z. Jiang, F.Y. Sun, L.Y. Cui, S.Q. Li, K.Q. Zhi, R.C. Zeng, Z.L. Wang, Corrosion resistance and antibacterial activity of hydroxyapatite coating induced by ciprofloxacin-loaded polymeric multilayers on magnesium alloy, Prog. Org. Coating 135 (2019) 465–474.
[34] H.A. Abd El-Rehim, E.A. Hegazy, F.H. Khalil, N.A. Hamed, Radiation preparation of drug carriers based polyacrylic acid (PAAc) using poly(vinyl pyrrolidone) (PVP) as a template polymer, Nucl. Instrum. Methods Phys. Res., Sect. B 254 (2007) 105–112.
[35] L.Y. Cui, R.C. Zeng, S.Q. Li, F. Zhang, E.H. Han, Corrosion resistance of layer-by-layer assembled polyvinylpyrrolidone/polyacrylic acid and amorphous silica films on AZ31 magnesium alloys, RSC Adv. 6 (2016) 63107–63116.
[36] J. Saqib, Isam H. Aljundi, Membrane fouling and modification using surface treatment and layer-by-layer assembly of polyelectrolytes: state-of-the-art review, J. Water Process Eng. 11 (2016) 68–87.
[37] J. Ma, J. Wang, X. Ai, S. Zhang, Biomimetic self-assembly of apatite hybrid materials: from a single molecular template to bi-/multi-molecular templates, Biotechnol. Adv. 32 (2014) 744–760.
[38] S. Kaabi Falahieh Asl, S. Nemeth, M.J. Tan, Improved corrosion protection of magnesium by hydrothermally deposited biodegradable calcium phosphate coating, Mater. Chem. Phys. 161 (2015) 185–193.
[39] L.Y. Cui, R.C. Zeng, S.K. Guan, W.C. Qi, F. Zhang, S.Q. Li, E.H. Han, Degradation mechanism of micro-arc oxidation coatings on biodegradable Mg-Ca alloys: the influence of porosity, J. Alloys Compd. 695 (2017) 2464–2476.
[40] Z.J. Jia, M. Li, Q. Liu, X.C. Xu, Y. Cheng, Y.F. Zheng, T.F. Xi, S.C. Wei, Micro-arc oxidization of a novel Mg-1Ca alloy in three alkaline KF electrolytes: corrosion resistance and cytotoxicity, Appl. Surf. Sci. 292 (2014) 1030–1039.
[41] S. Pu, M. Chen, Y. Chen, W. Zhang, H. Soliman, A. Qu, Q. Liu, X. Tang, N. Huang, G. Wan, Zirconium ions integrated in 1-hydroxyethylidene-1,1-diphosphonic acid (HEDP) as a metalorganic-like complex coating on biodegradable magnesium for corrosion control, Corrosion Sci. 144 (2018) 277–287.
[42] R.J. Kavitha, K. Ravichandran, T.S.N. Sankara Narayanan, Deposition of strontium phosphate coatings on magnesium by hydrothermal treatment: characteristics, corrosion resistance and bioactivity, J. Alloys Compd. 745 (2018) 725–743.
[43] J. Jayaraj, K.R. Rajesh, S. Amruth Raj, A. Srinivasan, S. Ananthakumar, N.G.K. Dhaipule, S.K. Kalpathy, U.T.S. Pillai, U.K. Mudali, Investigation on the corrosion behavior of lanthanum phosphate coatings on AZ31 Mg alloy obtained through chemical conversion technique, J. Alloys Compd. 784 (2019) 1162–1174.
[44] W. Yang, D. Xu, J. Wang, X. Yao, J. Chen, Microstructure and corrosion resistance of micro arc oxidation plus electrostatic powder spraying composite coating on magnesium alloy, Corrosion Sci. 136 (2018) 174–179.
[45] K. Cesarz-Andraczke, R. Nowosielski, M. Basiaga, R. Babilas, Study of the morphology and properties of biocompatible Ca-P coatings on Mg alloy, Materials 13 (2019) 2.
[46] Z. Li, Q. Ren, X. Wang, Q. Kuang, D. Ji, R. Yuan, X. Jing, Effect of phosphate additive on the morphology and anti-corrosion performance of plasma electrolytic oxidation coatings on magnesium-lithium alloy, Corrosion Sci. 157 (2019) 295–304.
[47] T.M. Mukhametkaliyev, M.A. Surmeneva, A. Vladescu, C.M. Cotrut, M. Braic, M. Dinu, M.D. Vranceanu, I. Pana, M. Mueller, R.A. Surmenev, A biodegradable AZ91 magnesium alloy coated with a thin nanostructured hydroxyapatite for improving the corrosion resistance, Mater. Sci. Eng. C 75 (2017) 95–103.
[48] S. Shen, S. Cai, Y. Li, R. Ling, F. Zhang, G. Xu, F. Wang, Microwave aqueous synthesis of hydroxyapatite bilayer coating on magnesium alloy for orthopedic application, Chem. Eng. J. 309 (2017) 278–287.
[49] X. Li, Z. Weng, W. Yuan, X. Luo, H.M. Wong, X. Liu, S. Wu, K.W.K. Yeung, Y. Zheng, P.K. Chu, Corrosion resistance of dicalcium phosphate dihydrate/poly(lactic-co-glycolic acid) hybrid coating on AZ31 magnesium alloy, Corrosion Sci. 102 (2016) 209–221.
[50] K. Xia, H. Pan, T. Wang, S. Ma, J. Niu, Z. Xiang, Y. Song, H. Yang, X. Tang, W. Lu, Effect of Ca/P ratio on the structural and corrosion properties of biomimetic CaP coatings on ZK60 magnesium alloy, Mater. Sci. Eng. C 72 (2017) 676–681.
[51] H. Yang, K. Xia, T. Wang, J. Niu, Y. Song, Z. Xiong, K. Zheng, S. Wei, W. Lu, Growth, in vitro biodegradation and cytocompatibility properties of nano-hydroxyapatite coatings on biodegradable magnesium alloys, J. Alloys Compd. 672 (2016) 366–373.
[52] P. Liu, J.M. Wang, X.T. Yu, X.B. Chen, S.Q. Li, D.C. Chen, S.K. Guan, R.C. Zeng, L.Y. Cui, Corrosion resistance of bioinspired DNA-induced Ca-P coating on biodegradable magnesium alloy, J. Magnes. Alloys 7 (2019) 144–154.
[53] G. Yang, Enhancing corrosion resistance, osteoinduction, and antibacterial properties by Zn/Sr additional surface modification of magnesium alloy, ACS Biomater. Sci. Eng. 4 (2018) 4289–4298.
[54] W. Yu, R. Sun, Z. Guo, Z. Wang, Y. He, G. Lu, P. Chen, K. Chen, Novel fluoridated hydroxyapatite/MAO composite coating on AZ31B magnesium alloy for biomedical application, Appl. Surf. Sci. 464 (2019) 708–715.
[55] S. Kaabi Falahieh Asl, S. Nemeth, M.J. Tan, Novel biodegradable calcium phosphate/polymer composite coating with adjustable mechanical properties formed by hydrothermal process for corrosion protection of magnesium substrate, J. Biomed. Mater. Res., Part B 104 (2016) 1643–1657.